Supporting information: Nonlinear nano-imaging of interlayer coupling in 2D graphene-semiconductor heterostructures

Wenjin Luo,[1,2] Renkang Song,[1] Benjamin G. Whetten,[2] Di Huang,[1] Xinbin Cheng,[1] Alexey Belyanin,[3,*] Tao Jiang,[1,†] and Markus B. Raschke[2,‡]

[1]*MOE Key Laboratory of Advanced Micro-Structured Materials,*
Shanghai Frontiers Science Center of Digital Optics,
Institute of Precision Optical Engineering,
and School of Physics Science and Engineering,
Tongji University, Shanghai 200092, China

[2]*Department of Physics and JILA, University of Colorado, Boulder, CO, 80309, USA*

[3]*Department of Physics and Astronomy, Texas A&M University,*
College Station, Texas 77843, United States

(Dated: December 12, 2023)

Fundamental excitation spectrum

Figure S1 shows the tip-scattered pump spectrum from a free-standing tip. The excitation spectrum spans from ∼785 to 900 nm and drives the FWM and 2PPL optical process. The short wavelength tail of the pump light (< 785 nm) is filtered out to enable detection of the FWM and 2PPL generated in that spectral range.
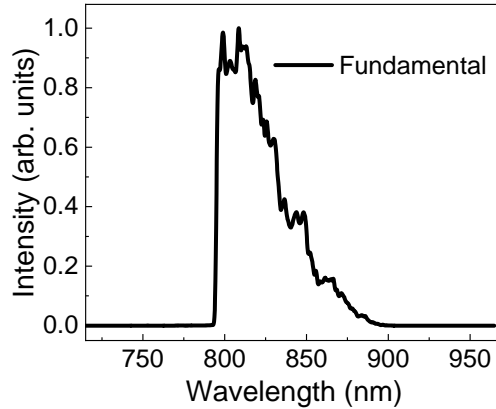

Fig. S1. Fundamental excitation spectrum from the tip apex.

Note 1: Resonant A-exciton FWM

To demonstrate the FWM enhancement, we compared our WSe_2 results to the FWM signal from MoS_2 in Ref. [1]. Compared to the higher A-exciton energy of MoS_2 which is further detuned from the Ti:sapphire pump photon energy, we observe stronger FWM from the WSe_2 as expected.

Note 2: Phonon resonances

The contribution from acoustic phonon resonances would affect the FWM signal in several different ways.

First, spontaneous electron-acoustic phonon scattering can contribute to the overall scattering rate, i.e. accelerate T_2 and thus affect the time integrated FWM signal intensity. However, this relaxation channel would contribute only weakly, as suggested also by our previous time resolved nano-imaging of electronic coherence in graphene [2] and WSe_2 [1], with result in good agreement with theory and consistent with a range of other experiments. Secondly, stimulated Brillouin scattering could contribute directly to the signal, but primarily on the red side of the fundamental (Stokes), whereas we observe FWM on the blue side. So far, we have not observed an efficient stimulated Brillouin scattering on the anti-Stokes side in graphene and TMDs in our own measurements or seen corresponding reports in the literature. Coherent generation of anti-

Stokes components in a CARS-like process is possible, but it would require a special arrangement, such as tuning to cavity resonances, or scattering off a dynamic grating formed by crossing pump beams. It would result in distinct peaks close to the fundamental frequency, not a broad featureless tail like we observe.

Resolution of nanoimaging

To characterize the nano-scale, sub-wavelength, and sub-diffraction localization of the nano-imaging, we show line profiles of zoomed-in scan nano-imaging from Fig. 2 from the main text. Fig. S2a-b show the FWM and 2PPL nano-imaging, and corresponding lines profiles along the dashed lines (Fig. S2c-e). The data indicate a spatial resolution of at least ~50 nm, assuming the underlying features to be sharp, and as defined by the 10-90 min-max standard.
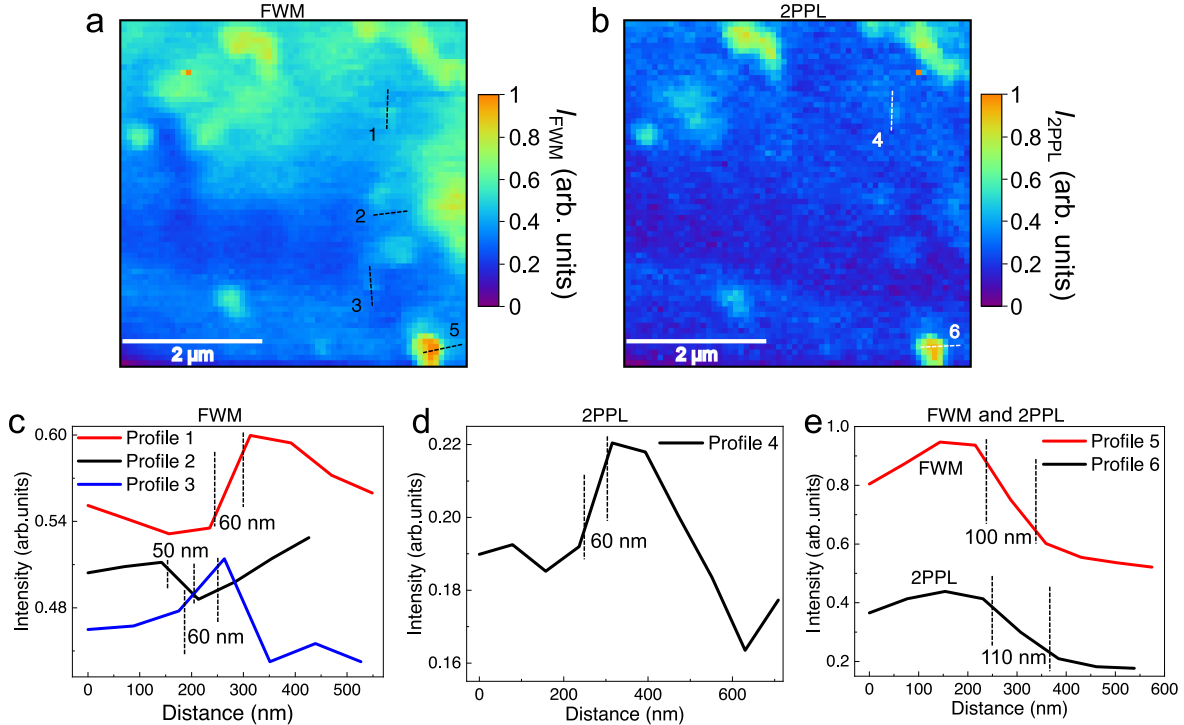

Fig. S2. (a-b) Zoomed-in nano-images of FWM and 2PPL from Fig. 2, with line profiles indicating near-field localization to ~50-100 nm, shown in (c-e).

Far-field WSe$_2$/graphene

We first fabricate a clean WSe$_2$/graphene heterostructure and pre-characterize it by FF-FWM and -2PPL imaging as shown in Fig. S3a-c, as well as AFM topography (Fig. 2c in the main text). The white dashed box indicates the nano-imaging area (Fig. 2) in the main text. The far-field

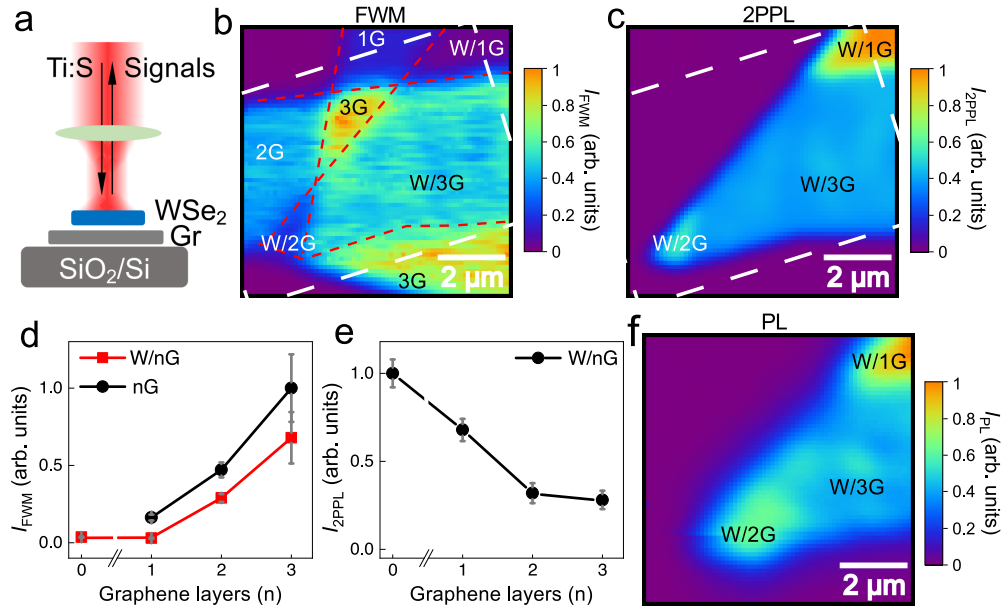FWM and 2PPL imaging both show smooth homogeneity and clear contrast in different areas of the whole sample.

Fig. S3. (a) Schematic of a far-field back-scattering geometry excitation on WSe$_2$ /graphene heterostructure. (b-c) Far-field FWM and 2PPL imaging, the red dashed lines indicate the physical boundaries of different areas, which are labeled. The thick dashed boxes indicate the nano-imaging area in the main text (Fig. 2). (d-e) Corresponding layer dependence of far-field FWM and PL intensity extracted from (b-c). (f) Corresponding far-field PL imaging with sample segments labeled.

We observed that the FWM from the heterostructure areas with WSe$_2$ covering graphene is weaker than that of pure graphene of equal thickness, the same trend as the 2PPL. The FWM and 2PPL trends are summarized in Fig. S3d-e, respectively, obtained from spatial averaging across the respective segments. Their FWM and 2PPL trends are similar to near-field results, but without the metal nano probe, there is no nano-cavity enhancement and the FWM intensity in W/3G areas is weaker than that of trilayer graphene (3G). Also, due to the lack of the additional non-radiative channel introduced by the metal tip, the 2PPL in W/2G and W/3G areas does not quench to zero, in contrast to the near-field case which quenches to effectively zero. We also characterize the PL of the sample (Fig. S3f), which shows similar results as the far-field 2PPL results.

Potential heterogeneity cases

We can envision several different types of potential large scale topological features, such as

bubbles and folds, as illustrated in Fig. S4. Folds and winkles would cause stacked layers of WSe$_2$ leading to stronger FWM intensities. The type-1 bubble case, due to the large gap between WSe$_2$ and graphene, would cause the local increase of the FWM signal. However, such an increase is not expected in the type-2 bubble case. In the contamination case, the nano-tip lifts off the WSe$_2$ as it scans over the contamination leading to the excitation source moving farther from the WSe$_2$ and causing weaker FWM. With our current methodology we cannot fully determine which cases cause the different strong and weak FWM responses we observe in areas with abnormal topography.
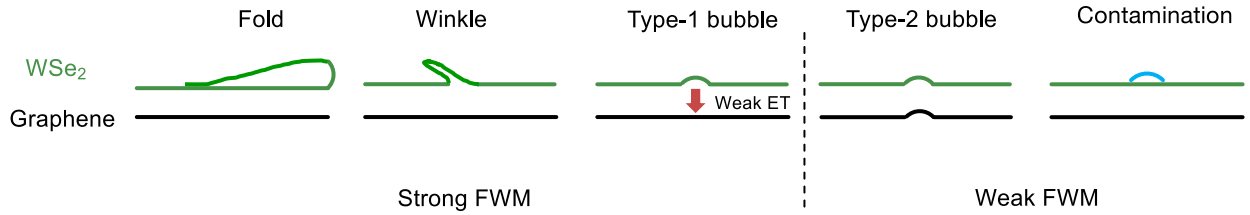

Fig. S4. Schematic of 5 different type of heterogeneity cases.

Far-field WSe$_2$ /hBN/graphene

As shown in the far-field FWM image in Fig. S5b, we observe that even with a spacer ($\sim$3.3 nm hBN) the FWM in the sandwich area (W/hBN/1G and W/hBN/2G) still decreases, we attribute this behavior to energy transfer through long-range Coulomb interactions. We observe under far-field conditions that the ratios of $\frac{I_{\mathrm{FWM}}(\mathrm{Gn})}{I_{\mathrm{FWM}}(\mathrm{W/nG})}$ and $\frac{I_{\mathrm{FWM}}(\mathrm{hBN/nG})}{I_{\mathrm{FWM}}(\mathrm{W/hBN/nG})}$ all are lower than under near-field conditions, which is consistent with the cases mentioned above, due to lack of the tip-graphene cavity enhancement. There is a higher FWM contrast in the near-field condition compared to the that of far-field due to the increased resolution from the nano-localized enhancement.
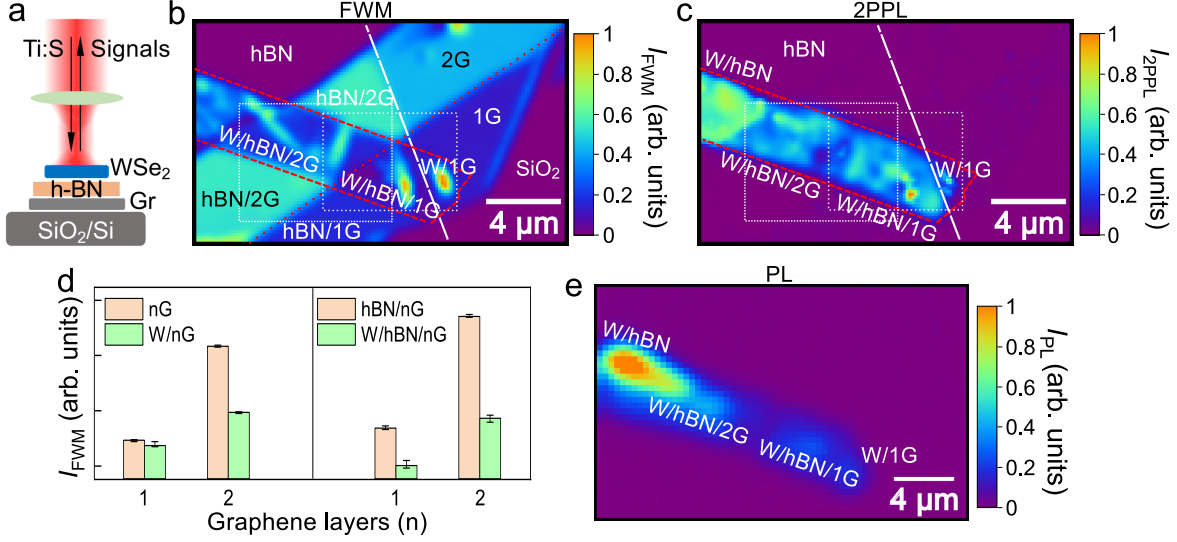
Fig. S5. Schematic of a far-field back-scattering geometry excitation on WSe$_2$/hBN/graphene heterostructure. (b-c) Far-field FWM and 2PPL imaging, the red dashed lines indicate the physical boundaries of different areas, which are labeled. The two white dashed boxes indicate the FWM nano-imaging area in the main text (Fig. 3b-c). (d) Corresponding layer dependence of far-field FWM intensity extracted from (b). (e) Corresponding far-field PL imaging with sample segments labeled.

Note 3: Rate equations

Based on the rate equations in Eq. 1 in the main text, the solution can be solved analytically in the steady state to find the distance dependence of exciton populations,

$$N_{\rm W} = \frac{F_{\rm W}}{\Gamma_{\rm W}^{\rm rad} + \Gamma_{\rm W}^{\rm nrad} + \Gamma_{\rm ET}^{\rm nrad}} \tag{1}$$

where subscript W stands for WSe$_2$. $\Gamma_{\rm W}^{\rm rad}$ is the intrinsic radiative decay rate in WSe$_2$. $\Gamma_{\rm W}^{\rm nrad}$ is the nonradiative decay rate due to the absorption of the near field in the tip and is expected to increase with decreasing tip-sample distance z. It then approaches a constant at large z, which is the intrinsic nonradiative decay rate in WSe$_2$ that does not depend on graphene or the tip. $\Gamma_{\rm ET}^{\rm nrad}$ is the nonradiative decay rate due to presence of graphene. Is is absent in the isolated WSe$_2$ case, and represents the energy transfer rate in the WSe$_2$/graphene case, which is expected to increase with the number of graphene layers. The 2PPL intensity for excitons is then given by

$$I_{\rm W} = \eta \Gamma_{\rm W}^{\rm rad} N_{\rm W} \tag{2}$$

here $\Gamma_{\rm W}^{\rm rad}$ is the radiative decay rate of excitons and η is the outcoupling efficiency from the cavity formed by the tip and the sample into the far field. In the near-field experiment, $\Gamma_{\rm W}^{\rm rad}$ may exhibit a

small dependence on tip-sample distance due to Purcell enhancement in the WSe_2 /graphene case, which we neglect in our model. Therefore, to minimize the number of uncertain parameters we treat the product $\eta \Gamma_W^{rad}$ as one z-dependent function.

The FWM intensity is determined by coherent addition of nonlinear currents $j^{(3)}$ from each layer (WSe_2 , graphene, substrate). Each current scales as

$$j^{(3)} \propto \chi^{(3)} E^3 \tag{3}$$

where E is the excitation field in a particular layer. Both the excitation field and the outgoing FWM signal field are strongly affected by the tip and the changing boundary conditions due to graphene. Our previous work shows an example of the effect of boundary conditions on the FWM field intensity [3].

It is worth mentioning that we believe the local maximum in Figure 4d-e at around 15 nm is due to intermittent formation of a water meniscus on the sample, modifying the local near-field distribution and intensity. The parameters for fitting the WSe_2 /graphene case versus the bare WSe_2 case are: l: 2 versus 1.5, D: 6 versus 4, δz: 0.5 versus 0.3 nm, and R for both cases are 14 nm.

In the z-scan approach curves shown in Figure 4b-e, the steeper rise of the FWM and its subsequent quenching over a shorter distance than the 2PPL is because of the 3rd versus 2nd order nonlinearities, which changes the crossover point at which the non-radiative decay outcompetes the radiative decay, despite the fact that both signals follow the same non-radiative power law. Interestingly, the maximum in the FWM curve of the heterostructure in Figure 4c does not occur at significantly shorter distances than the maximum of the 2PPL curve shown in Figure 4b like it does in the isolated WSe_2 case (Figure 4d-e). This may be due to a weak Purcell-enhancement in the heterostructure that is not accounted for in Eqs. 1-2. Because graphene is a semimetal, when placed under the WSe_2 layer it couples with the tip to form a leaky plasmonic cavity that can increase the 2PPL radiative decay rate through Purcell enhancement [4]. In contrast, with the absence of graphene for the data in Figure 4d-e, and only a dielectric SiO_2 substrate, no Purcell enhancement is expected. For our model, we have assumed that any Purcell enhancement can be neglected when compared to the effect of the tip-enhanced excitation rate F_W, due to the extremely low quality factor of a graphene-tip cavity leading to only small Purcell enhancement factors. Nevertheless, the matching locations of the maxima in the 2PPL and FWM curves in Figure 4b-c could be explained by such a small Purcell enhancement effect causing Γ_W^{rad} to increase

7

at short distances. While this cavity-induced Purcell enhancement would increase $\Gamma_{\mathrm{W}}^{\mathrm{rad}}$, the non-radiative rate $\Gamma_{\mathrm{W}}^{\mathrm{nrad}}$ would remain unchanged, and thus the maximum 2PPL value would occur at slightly shorter distances than it would otherwise, in this case causing it to approximately align with the FWM maximum.

References

[1] W. Luo, B. G. Whetten, V. Kravtsov, A. Singh, Y. Yang, D. Huang, X. Cheng, J. Tao, A. Belyanin, M. B. Raschke, *Nano Lett.* **2023**, *23*, 1767.

[2] T. Jiang, V. Kravtsov, M. Tokman, A. Belyanin, M. B. Raschke, *Nat. Nanotechnol.* **2019**, *14*, 838.

[3] S. Almutairi, Q. Chen, M. Tokman, A. Belyanin, *Phys. Rev. B* **2020**, *101*, 235156.

[4] M. A. May, T. Jiang, C. Du, K.-D. Park, X. Xu, A. Belyanin, M. B. Raschke, *Nano Lett.* **2020**, *21*, 522.